3D printed microchannel networks to direct vascularisation during endochondral bone repair

Andrew C. Daly[*], [1,2] Pierluca Pitacco[*], [1,2] , Jessica Nulty [1,2], Gráinne M. Cunniffe, [1,2] Daniel J. Kelly, [1,2,3,4 #]

[1]Trinity Centre for Bioengineering, Trinity Biomedical Sciences Institute, Trinity College Dublin, Dublin, Ireland.

[2]Department of Mechanical and Manufacturing Engineering, School of Engineering, Trinity College Dublin, Dublin, Ireland.

[3]Department of Anatomy, Royal College of Surgeons in Ireland, Dublin, Ireland

[4]Advanced Materials and Bioengineering Research Centre (AMBER), Royal College of Surgeons in Ireland and Trinity College Dublin, Dublin, Ireland.

*Both authors contributed equally to this work

[#]Corresponding Author: Tel: +353-1-8963947, email: kellyd9@tcd.ie

Abstract:

Bone tissue engineering strategies that recapitulate the developmental process of endochondral ossification offer a promising route to bone repair. Clinical translation of such endochondral tissue engineering strategies will require overcoming a number of challenges, including the engineering of large and often anatomically complex cartilage grafts, as well as the persistence of core regions of avascular cartilage following their implantation into large bone defects. Here 3D printing technology is utilized to develop a versatile and scalable approach to guide vascularisation during endochondral bone repair. First, a sacrificial pluronic ink was used to 3D print interconnected microchannel networks in a mesenchymal stem cell (MSC) laden gelatin-methacryloyl (GelMA) hydrogel. These constructs (with and without microchannels) were next chondrogenically primed *in vitro* and then implanted into critically sized femoral bone defects in rats. The solid and microchanneled cartilage templates enhanced bone repair compared to untreated controls, with the solid cartilage templates (without microchannels) supporting the highest levels of total bone formation. However, the inclusion of 3D printed microchannels was found to promote osteoclast/immune cell invasion, hydrogel degradation, and vascularisation following implantation. In addition, the endochondral bone tissue engineering strategy was found to support comparable levels of bone healing to BMP-2 delivery, whilst promoting lower levels of heterotopic bone formation, with the microchanneled templates supporting the lowest levels of heterotopic bone formation. Taken together, these results demonstrate that 3D printed hypertrophic cartilage grafts represent a promising approach for the repair of complex bone fractures, particularly for larger defects where vascularisation will be a key challenge.

Keywords: 3D printing, bioprinting, vascularisation, Endochondral, bone repair,

1 Introduction

The repair of large bone defects remains a significant challenge, and despite a number of drawbacks, autografting remains the clinical gold standard treatment option [1]. This has led to increased interest in tissue engineering and regenerative medicine approaches that are capable of promoting the repair of critically sized bone defects. Delivery of recombinant human osteoinductive growth factors such as BMP-2 offers one of the most successful bone engineering strategies to date, as evidenced by extensive animal and clinical studies that have demonstrated its ability to induce bone formation [2–6]. The FDA has approved the use of the INFUSE® Bone Graft (BMP-2) to support bone growth in a number of clinical scenarios. The potency of BMP-2 delivery has been shown to be dose dependent, with higher doses generally resulting in higher levels of bone formation [7,8]. In clinical situations "off label" supra-physiological doses are often used to effectively induce bone formation [9,10] . However, increasing pre-clinical and clinical data has demonstrated that the use of supra-physiological doses can have a number of side effects such as excess inflammation [11], heterotopic ossification [12,13] and structurally abnormal bone formation [7]. This has led to increased interest in alternative bone tissue engineering strategies.

Traditionally the field of bone tissue engineering has focused on the direct generation of bone by inducing osteogenic differentiation of mesenchymal stem cells (MSCs) or osteoprogenitors cells, which recapitulates the developmental process of intramembranous ossification. More recently, tissue engineering strategies that recapitulate the developmental process of endochondral ossification, whereby cartilage intermediaries are replaced by bone, have received increased interest in the field [14]. It has been demonstrated that cartilage tissues, engineered using MSCs, can act as templates for endochondral bone formation *in vivo* [15–19]. A number of studies have now demonstrated that it is possible to repair large bone defects in rodent

models using such endochondral approaches [20–23]. However, a number of challenges must be addressed before these approaches can be adopted in a clinical setting. Firstly, strategies are required to engineer large and often anatomically complex cartilage grafts that match the geometry of the bone defect to be treated. Furthermore, although it has been shown that cartilage templates become well vascularised *in vivo* [16,18,24], vascularisation proceeds from peripheral regions, with avascular cartilage persisting in core regions of scaled up constructs [25,26]. Therefore, strategies that can accelerate and direct vascularisation within hypertrophic cartilage templates will be required to successfully scale up these approaches to clinical dimensions.

The adoption of 3D-printing technology in tissue engineering has made it possible to pattern constructs with templated internal and external architectures [27–30]. We hypothesize that 3D-printing technology could be used to engineer geometrically complex hypertrophic cartilage templates with controlled internal architectures to guide vascularisation during endochondral bone repair. In this study, a sacrificial pluronic ink is used to pattern interconnected microchannel networks inside MSC laden gelatin-methacryloyl (GelMA) hydrogels. The approach is versatile making it possible to print a range of different microchannel diameters in arbitrary complex geometries. The utility of the printed microchannels was assessed by implanting chondrogenically primed hydrogels (with and without microchannel networks) into critically sized femoral bone defects in rats. After 4 & 8 weeks, vascularisation and bone formation was assessed using a combination of histological and μCT analysis. As a positive control, GelMA hydrogels containing a clinically relevant rhBMP-2 dose (0.2 mg/ml, 12.4 μg/defect) were also implanted into the defects.

2 Methods

2.1 Isolation and expansion of MSCs

Bone marrow derived MSCs were isolated from the femoral shaft of 6 week old rats (Fischer Male) and expanded in high-glucose Dulbecco's modified Eagle's medium GlutaMAX (hgDMEM) supplemented with 10% v/v fetal bovine serum (FBS), 100 U/ml penicillin, 100 µg/ml streptomycin (all Gibco Biosciences, Dublin, Ireland) and 2.5 µg/ml amphotericin B (Sigma–Aldrich, Dublin, Ireland) at 5% pO2. Following colony formation, MSCs were trypsinized, counted, seeded at density of 5000 cells cm^2 in 500 cm^2 triple flasks (Thermo Fisher Scientific), supplemented with hgDMEM, 10% v/v FBS, 100 U/ml penicillin, 100 µg/ml streptomycin, 2.5 µg/ml amphotericin B, and 5 ng/ml human fibroblastic growth factor-2 (FGF-2; Prospec-Tany TechnoGene Ltd., Israel) and expanded to passage 2 at 5% pO2.

2.2 GelMA Synthesis

Gelatin methacryloyl (GelMA) was synthesized by reaction of porcine type A gelatin (Sigma Aldrich, Bloom number 175, average molecular mass 40-50 kDa) with methacrylic anhydride (Sigma Aldrich) at 50 °C for four hours, as previously described [31]. Methacrylic anhydride was added to a 10% solution of gelatin in PBS under constant stirring. To achieve a high degree of functionalization, 1 ml of methacrylic anhydride was added per gram of gelatin. This protocol has been shown to support a degree of metacrylation of approximately 75% [32,33]. The functionalized polymer was dialyzed against distilled water for 7 days at 40 °C to remove methacrylic acid and anhydride, freeze-dried and stored at -20 °C until use.

2.3 In vitro culture conditions

The chondrogenic culture conditions applied in this study are defined as culture in a chondrogenic medium (CDM) consisting of hgDMEM GlutaMAX supplemented with 100 U/ml penicillin, 100 µg/ml streptomycin, 100 µg/ml sodium pyruvate, 40 µg/ml L-proline, 50 µg/ml L-ascorbic acid-2-phosphate, 4.7 µg/ml linoleic acid, 1.5 mg/ml bovine serum albumine, 1 X insulin–transferrin–selenium, 100 nM dexamethasone (all from Sigma–Aldrich), 2.5 µg/ml amphotericin B, 500 ng/ml of recombinant human bone morphogenetic protein 2 (BMP-2) (Peprotech, EC Ltd) and 10 ng/ml of human transforming growth factor- β 3 (TGF- β 3) (Prospec-Tany TechnoGene Ltd., Israel). The constructs were primed for 2 weeks at 5% pO_2 followed by 2 weeks at 20% pO_2 before implantation.

2.4 3D-Printing system

Pluronic F127 (Sigma Aldrich, MW 12.6 kDa) was dissolved at 40wt% in deionized ultrapure water by mixing at 4° overnight. The ink was loaded into a syringe and centrifuged to remove any air bubbles, and then printed at 18°C, using a 30G needle, and an extrusion pressure of 0.5 MPa. Note the printing platform was not heated. At this temperature the ink exhibits sufficient shear thinning behaviour to print in a controlled manner [34]. All 3D-printing was performed using a 3D Discovery system (Regen Hu, Switzerland). A GelMA concentration of 10 wt% (including irgacure 0.05 wt %) was used throughout. Cross-linking was performed using UV light for 25 mins (365 nm, 5 mW/cm^2), and a cell density of 20 million BMSCs/ml of hydrogel was used throughout. Further details on construct fabrication and the 3D-printing parameters are provided in section 3.1.

2.5 Biochemical analysis

The biochemical content of all hydrogels were analysed pre-implantation after 4 weeks of *in vitro* culture. Prior to biochemical analysis, constructs were washed in PBS, weighted and frozen for subsequent assessment. Each construct was digested with papain (125 μg/ml) in 0.1M sodium acetate, 5mML-cysteine–HCl, 0.05 methylenediaminetetraacetic acid (EDTA), pH 6.0 (all from Sigma–Aldrich) at 60 °C and 10 rpm for 18 h. DNA content was quantified using the Hoechst Bisbenzimide 33258 dye assay, with a calf thymus DNA standard. The amount of sulphated glycosaminoglycan (sGAG) was quantified using the dimethyl methylene blue dye-binding assay (Blyscan, Biocolor Ltd., Northern Ireland), with a chondroitin sulphate standard.

2.6 Histological and Immunohistochemical analysis

Constructs were fixed in 4% paraformaldehyde, dehydrated in a graded series of ethanol's, embedded in paraffin wax, sectioned at 8 μm and affixed to microscope slides. Post-implantation constructs were decalcified in EDTA for 2 weeks. The sections were stained with haematoxylin and eosin (H&E) to assess bone formation and safarin-O to assess sGAG content. Collagen types I, II and X were evaluated using a standard immunohistochemical technique; briefly, sections treated with chondroitinase ABC (Sigma-Aldrich) in a humidified environment at 37°C to enhance permeability of the extracellular matrix. Sections were incubated with goat serum to block non-specific sites and collagen type I (ab90395, 1:400), collagen type II (ab3092, 1:100) or collagen type X (ab49945, 1:200) primary antibodies (mouse monoclonal, Abcam, Cambridge, UK) were applied for 24 h at 4º. Next, the sections were treated with peroxidase to block endo-peroxidise activity. Next, the secondary antibody (Coll II & I, anti-Mouse IgG, B7151, 1.5:200; Coll X, anti-IgM, ab49760, 1:200) was added for 1h at room temperature followed by incubation with ABC reagent (Vectastain PK- 400, Vector Labs, Peterborough, UK) for 45 min. Finally, sections were

developed with DAB peroxidase (Vector Labs) until brown staining was observed in the positive controls. Note, if brown staining was observed in the negative controls for this time period the staining was repeated until corrected. To evaluate host immune cell invasion sections were assayed for cellular expression of tartrate-resistant acid phosphatase (TRAP) using an acid phosphatase staining kit (acid phosphatase leukocyte TRAP kit, Sigma).

2.7 Live/dead confocal microscopy

Cell viability was assessed after 24 h using a LIVE/DEAD™ viability/cytotoxicity assay kit (Invitrogen, Bio-science, Ireland). Briefly, constructs were washed in PBS followed by incubation in PBS containing 2 μM calcein AM (green fluorescence of membrane for live cells) and 4 μM ethidium homodimer-1 (red fluorescence of DNA for dead cells; both from Cambridge Bioscience, UK). Sections were again washed in PBS, imaged with a Leica SP8 scanning confocal at 515 and 615 nm channels, and analysed using Leica Application Suite X (LAS X) software.

2.8 Surgical procedure

Critically-sized (5 mm) femoral defects were created in immune-competent adult Fischer rats (>12 weeks old) following an established procedure [35,36]. Constructs were press-fit into the defect site, and repair tissue was harvested for analysis at 4 and 8 weeks post-implantation. One defect was created per animal and n = 9 constructs were implanted per time point. A total of 72 rats were used for the study; 18 rats received either no construct (Empty), a chondrogenically primed solid construct (Solid endochondral ossification (EO)), a chondrogenically primed channelled construct (Microchannels EO), or a BMP-2 loaded solid construct with no pre-culture (BMP-2). This animal procedure and study was approved by the ethics committee in the Trinity College Dublin and the health products regulatory authority (HPRA) in Ireland. Briefly, anaesthesia was induced and

maintained by isoflurane-oxygen throughout the surgery. The rats were also injected with buprenorphine to provide pain relief during and after surgery. The shaft of the left femur was exposed by dissections and the periosteum was scraped back to allow access to the bone. A weight-bearing polyetheretherketone (PEEK) internal fixation plate was secured to the exposed femur with four screws into pre-drilled holes. A 5 mm mid-diaphyseal defect was then created using a dental drill fitted with 2 small circular parallel saw blades welded to a narrow straight rod separated with a 5 mm spacer. The defect site was thoroughly irrigated with saline to remove bone debris before it was treated with a construct. The wounds were closed with sutures and the rats were allowed to recover. On dates of scheduled explant retrieval, rats were sacrificed by CO_2 asphyxiation. The repaired femur, with the PEEK plate fixator intact, was carefully separated from the adjacent hip and knee joints for analysis.

2.9 Vascular CT Analysis

Contrast enhanced angiography was performed at week 4 to assess vascularisation within the bone defects. First, the rat was sacrificed using CO_2 asphyxiation. Next, the vasculature was immediately perfused through the ascending aorta with sequential solutions of heparin (25 U/ml), formalin, PBS, and a barium-based contrast agent. The contrast agent was composed of porcine type A gelatin (3 wt%), sodium chloride (0.9 wt%) and barium powder (40 wt%; Sigma B8675). All solutions were thoroughly mixed before perfusion and maintained at 37°C for the duration of the perfusion procedure. A straight 18G intravenous catheter was used to deliver the perfusion solutions into the rats left ventricle. A peristatic pump was used to deliver the heparin, formalin, and PBS solutions at a rate of 6 ml/min. The contrast agent was delivered at a rate of 3 ml/min. After perfusion, the limbs were excised and scanned using μCT (as described above) with both bone and contrast agent present. Scans were performed using a voltage of 70 kVp, and a current

of 114 µA. A Gaussian filter (sigma = 0.8, support = 1) was used to suppress noise and a global threshold of 210 corresponding to a density of 399.5 mg hydroxyapatite/cm^3 was applied. A voxel resolution of 15.6 µm was used throughout. To facilitate visualisation and quantification of the vascular volume alone, the excised limbs were next decalcified in EDTA (15 wt%, pH 7.4) for 2 weeks to remove the bone mineral content. µCT scans were performed before and after decalcification. By comparing the two scans (pre and post decalcification) it was possible to define the defect VOI by using the relative position of the fixation screws present in both scans. Next, 3D evaluations was carried out on the segmented images to determine vascular volume and to reconstruct a 3D image. The vascular volume in the defect was quantified by measuring the total quantity of x-ray attenuating contrast agent in the central 288 (4.5 mm) slices of the defect. The vascular volume present in the core of the defect was analysed by defining a Ø2mm VOI in the defect. The vessel thickness, degree of anisotropy and connectivity were analysed using trabecular thickness analysis scripts provided by SCANCO that fit a maximal sphere in either the pore or trabecular strut at each voxel in 3D space.

2.10 In vivo µCT analysis

µCT scans were performed on constructs using a Scanco Medical vivaCT 80 system (Scanco Medical, Bassersdorf, Switzerland). Rats (n=9) were scanned at 2, 4, 6 and 8 weeks post-surgery to assess defect bridging and bone formation within the defect. First, anaesthesia was induced in an induction chamber. Next, the rats were placed inside the vivaCT scanner and anaesthesia was maintained by isoflurane-oxygen throughout the scan. Next, a radiographic scan of the whole animal was used to isolate the rat femur. The animal's femur was aligned parallel to the scanning field-of-view to simplify the bone volume assessments. Scans were performed using a voltage of 70 kVp, and a current of 114 µA. A Gaussian filter (sigma = 0.8, support = 1) was used to suppress

noise and a global threshold of 210 corresponding to a density of 399.5 mg hydroxyapatite/cm^3 was applied. A voxel resolution of 35 µm was used throughout. 3D evaluation was carried out on the segmented images to determine bone volume and density and to reconstruct a 3D image. Bone volume and bone density in the defects was quantified by measuring the total quantity of mineral in the central 130 slices of the defect. To differentiate regional differences in bone formation three volumes of interest (VOI) were created. Concentric Ø2mm, Ø4mm and Ø10mm were aligned with the defect and used to encompass bone formation. The VOIs were aligned using untreated native bone along the femur. The core bone volume was quantified from the inner Ø2mm VOI. The annular bone volume was quantified by subtracting the Ø2mm VOI from the Ø4mm VOI. Heterotopic bone volume was quantified by subtracting the Ø4mm VOI from the Ø10mm VOI. The bone volume percentages for each region were then calculated by dividing the corresponding bone volume (i.e. bone volume in the annulus) by the total bone volume in the defect. The variance of bone density with depth through the constructs was analysed qualitatively by examining sections at a depth of 25%, 50% and 75% from the top of the construct (one-quarter, mid and three-quarter sections). The bone volume and densities were then quantified using scripts provided by Scanco.

2.11 Mechanical characterisation

Samples were tested in unconfined compression using a standard materials testing machine (Zwick Roell Z005; Herefordshire) with a 5N load cell. Stress tests were performed with a ramp displacement of 1 mm/s until 10% strain. The young's modulus in compression was assessed using stress tests where the samples were compressed with a ramp displacement of 1 mm/s until 10% strain. The modulus was taken as the slope of the stress strain curve between 0%–10% strain.

2.12 Statistical analysis

Statistical analyses were performed using ANOVA throughout, with tukey's test for multiple comparisons used to compare conditions. Significance was accepted at a level of $p \leq 0.05$. Numerical and graphical results are presented as mean ± standard deviation, with graphical results produced using GraphPad Prism (Version 6.02).

3 Results

3.1 3D printing of microchanneled cartilage templates

We first looked to establish a method for 3D-printing templated hydrogels containing an internal architecture of interconnected channels. To this end, a free-standing network of micropillars was 3D-printed onto a glass slide using a pluronic ink (40 wt%) (Fig 1 a; video 1). The micropillars could be extruded vertically into the z-plane, and horizontally into the xy-plane, in a highly controlled manner. At 18° the pluronic ink exhibits sufficient shear thinning behaviour to print complex overhanging structures which can support their own weight (Fig 1a). For temperatures below 18°C shear thinning behaviour was lost, and it was not possible to print the micropillar network. Next, a pluronic circle (4 mm inner-Ø) was printed around the micropillars (Fig 1a). A cell-laden GelMA solution (10 wt% + irgacure 0.05 wt %), containing MSCs (20 million/ml), was pipetted around the micropillars and then cross-linked using UV light for 25 mins (365 nm, 5 mW/cm^2). Solid constructs were fabricated by casting the GelMA - MSC solution into a pluronic circle containing no micropillars. For the solid and microchanneled constructs, solution volumes of 62µl (1.24 million BMSCs) and 44µl (0.88 million BMSCs) were pipetted respectively. The constructs were next placed in CDM media at 37°C for 3 hours. The pluronic network was then sacrificed by cooling the constructs in 4°C media for 5 minutes, which resulted in the formation of an open network of interconnected microchannels inside the cylindrical hydrogel (Fig 1 b). The microchannel diameter could be varied from to ~265 µm up to ~1225 µm by changing the printing translation speed from 1 mm/s - 6 mm/s. An extrusion speed of 1.5 mm/s was used for the central pillar (~900 µm Ø), and an extrusion speed of 4 mm/s was used for the 4 outer pillars and all horizontal pillars (365 µm Ø) (Fig 1 c). The young's modulus in compression of the printed hydrogel structures was 76 ± 4 kPa for the solid constructs, and 69 + 15 kPa for the

microchanneled constructs. Live/dead staining, 24 hours post-fabrication, indicated that MSCs remained viable within the GelMA hydrogel (Fig 1 d). It was also possible to leverage the approach to print anatomically shaped constructs containing microchannels (Fig 1 e). To do this, a negative mold generated from a µCT scan of a human humeral head was printed using a pluronic ink. Next, a network of micropillars were printed into the mold. Like before, it was possible to cast the GelMA hydrogel and sacrifice the pluronic ink to create a network of internal microchannels.

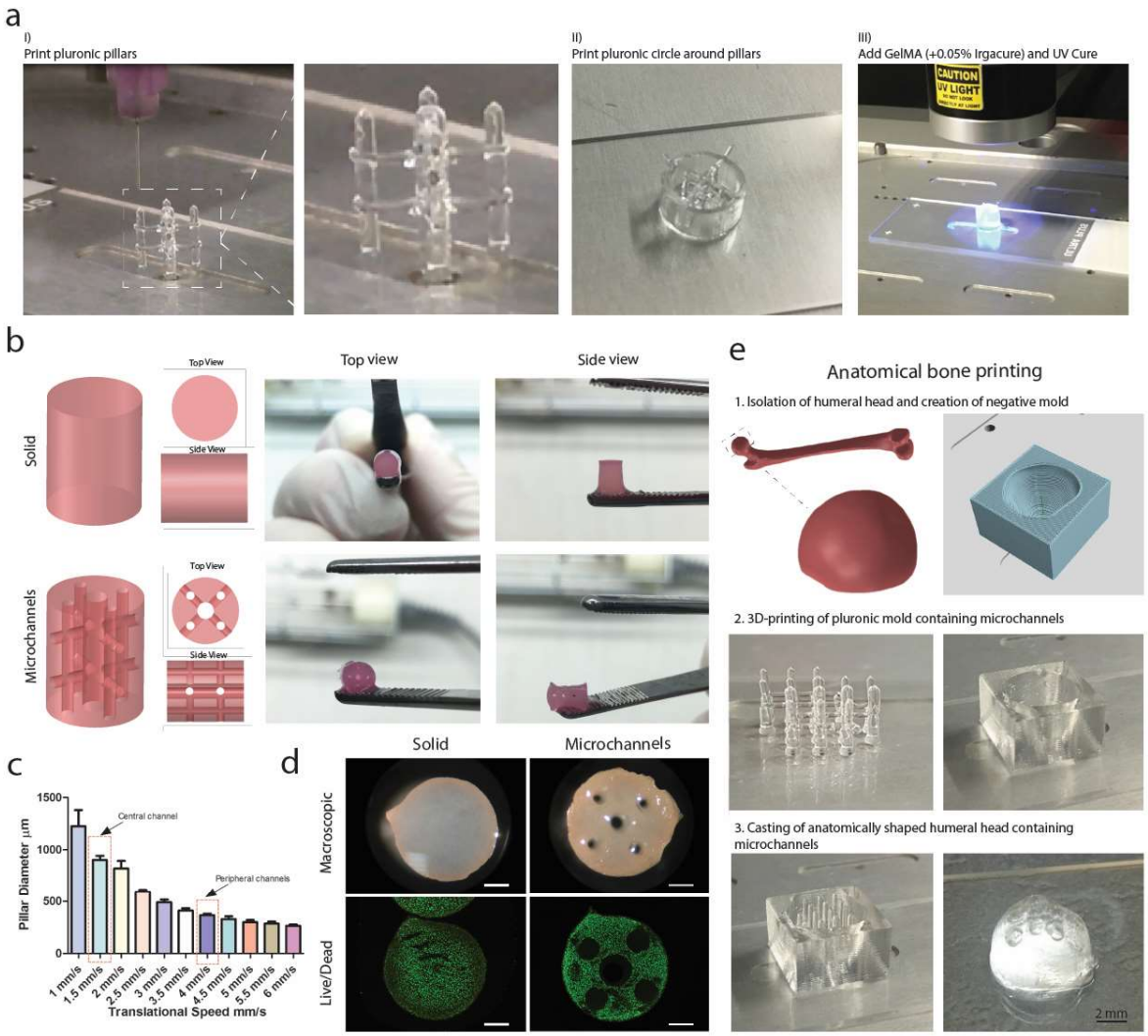

Figure 1: 3D-printing of microchanneled hydrogels. (a) Outline of 3D printing process, i) printing of pluronic micropillars, ii) printing of pluronic circle around the micropillars and iii) UV curing of GelMA/MSC solution around the micropillars. (b) Outline of construct design (solid and microchanneled), top and side views demonstrating interconnected microchannel network within the constructs. (c) Pillar diameter (μm) as a function of printhead translation speed (mm/s). (d) Macroscopic images and live/dead staining 24 hours post-fabrication, scale-bar 500 μm. E) Anatomically accurate bone printing process, generation of mold using CT data, 3D-printed pluronic mold and micropillars in separation and isolation, cast GelMA hydrogel containing microchannels, scale-bar 2 mm.

Post-fabrication, the constructs were chondrogenically primed *in vitro* for 4 weeks to engineer solid and microchanneled cartilage templates (Fig 2 a). Biochemical analysis along with immunohistochemical staining for type II collagen at the end of the 4 week *in vitro* culture period demonstrated that MSCs had undergone chondrogenesis within the GelMA hydrogel (Fig 2 b, c). Weak staining for collagen X was observed in both groups (Fig 2 c). As expected, the total DNA content was higher in the solid constructs as the empty microchannels occupy approximately 30% of the construct volume (Fig 2 b). sGAG synthesis (sGAG/DNA) was comparable in both groups (Fig 2 b). Next, the chondrogenically primed hydrogels were implanted into critically-sized 5 mm femoral defects in rats (Fig 2 a). As a positive control, GelMA hydrogels containing rhBMP-2 (0.2 mg/ml GelMA solution, 12.4 μg/defect) were implanted. To confirm the defects were critically sized, empty defects that received no implants were also included.

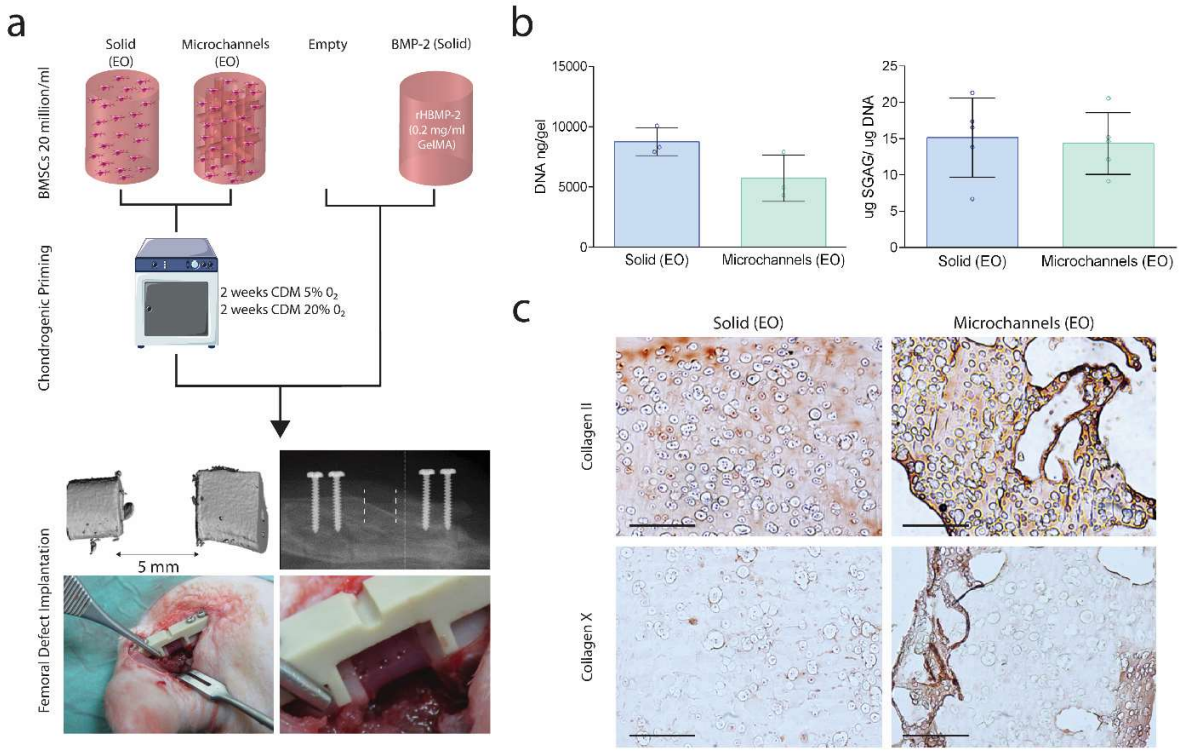

Figure 2: Experimental outline and pre-implantation analysis. (a) Outline of experimental groups (solid and microchanneled) and control groups (empty and BMP-2); pre-implantation chondrogenic culture conditions; and implantation of primed hydrogel (channelled) into a 5 mm femoral defect. (b) Biochemical analysis (Total DNA/construct (n=3) and sGAG/DNA (n=5) of both groups after 4 weeks of in vitro culture. (c) Immunohistochemical staining for collagen II pre-implantation, 4X scale-bar 1 mm.

3.2 µCT angiography to assess vascular network formation

4 weeks post-implantation, µCT angiography was used to quantify and visualise vascular network formation in the defects. 3D reconstructions revealed extensive vascular networks had formed within the defect (Fig 3 a). No significant differences in total vascular volume, vessel connectivity or mean vessel thickness were observed between the experimental groups; however, the vessel anisotropy was significantly higher in the BMP-2 group compared to solid endochondral ossification (EO) group (Fig 3 b). Next, we performed region of interest analysis to quantify the

levels of vascularisation within the defect core (2 mm Ø), and found there was a trend towards higher levels of vascularisation within core regions of the microchanneled cartilage templates (p=0.07 versus solid EO) (Fig 3 c).

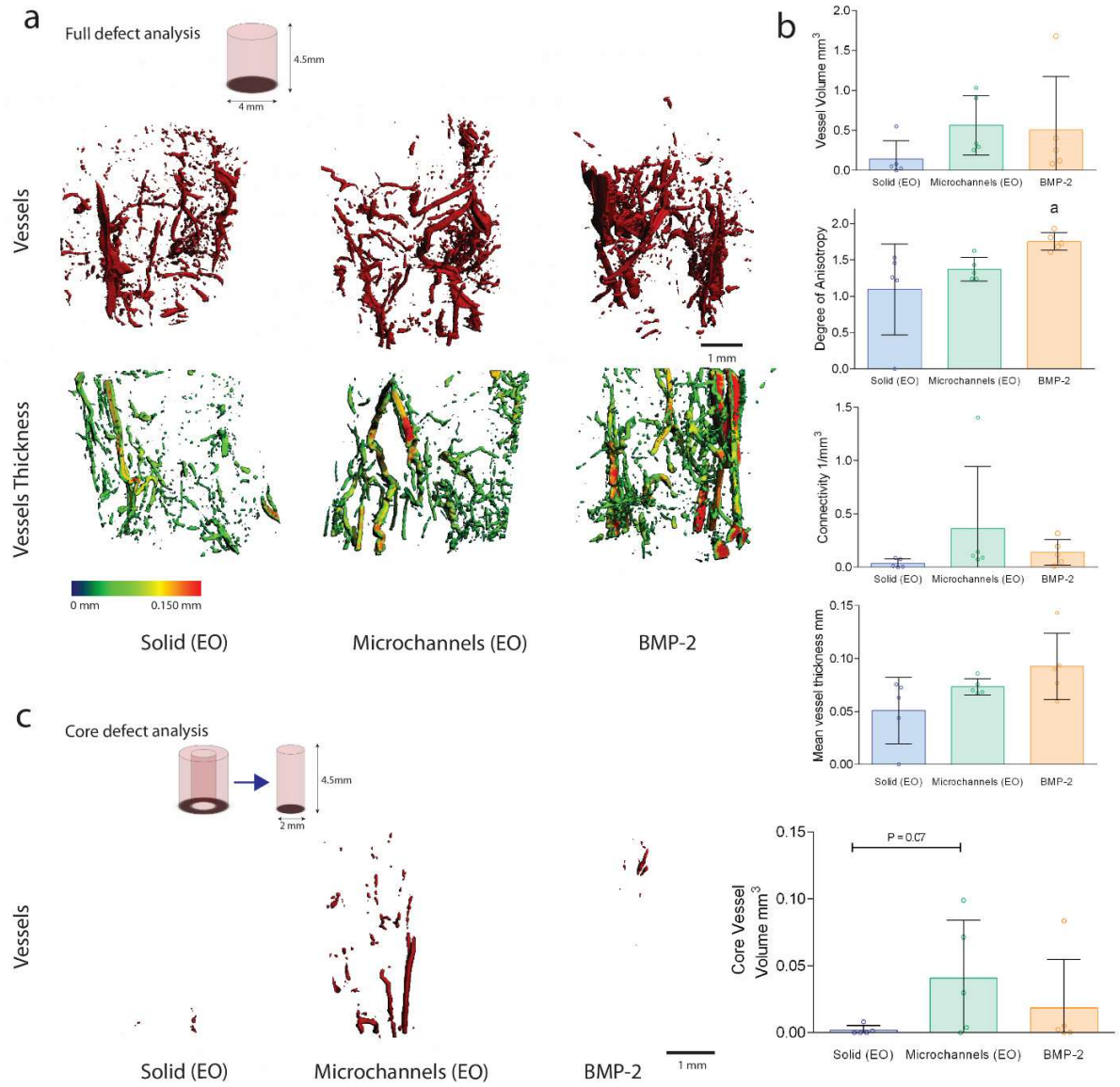

Figure 3: µCT angiography following 4 weeks of *in vivo* implantation. (a) Representative 3D reconstructions of vessel formation for each group along with corresponding 3D morphometric reconstructions of vessel diameters within the defects. (b) Quantification of total vessel volume, degree of vessel anisotropy, vessel connectivity and mean vessel

thickness for all groups, “a” denotes significance compared to solid (EO). (c) Representative 3D reconstructions of vessels within the defect core (2 mm Ø) for each group. Quantification of total vessel volume within the core of the defect. All graphs n=5 (mean ± SD) throughout, significance defined as $p < 0.05$ (ANOVA).

3.3 In Vivo μCT analysis of bone volume and bone density

Next, μCT analysis was used to visualise and quantify bone formation within the defects after 2, 4, 6, and 8 weeks of implantation (Fig 4 a). Over the 8 week period, the total bone volume in the defects increased for all experimental groups (Fig 4 a, c). Compared to the empty untreated group which as expected failed to bridge, a significantly higher total bone volume was present in all experimental groups after 8 weeks (Fig 4 a, c). After 6 & 8 weeks of implantation, a significantly higher bone volume was present in the solid (EO) and BMP-2 delivery groups compared to the microchanneled (EO) templates (Fig 4 c). No significant difference in total bone volume was found between the solid (EO) and BMP-2 delivery group at any timepoint (Fig 4 c). Bone density mapping demonstrated cortical-like bone, with a density comparable to the adjacent native bone (~1200 mg HA/cm^3), had formed within the defects after 8 weeks (Fig 4 b). Quantitative densitometry analysis revealed the average bone density (mg HA/cm^3) within the microchanneled cartilage group was significantly higher after 4 weeks (Fig 4 d). Next we assessed the kinetics of bone formation between timepoints (Fig 4 e). This revealed that the highest levels of bone formation occurred between weeks 2 and 4 for the BMP-2 delivery group, with lower levels produced between weeks 4 and 8. In contrast, bone formation following implantation of both the solid and microchanneled cartilage templates was more consistent over time (Fig 4 e).

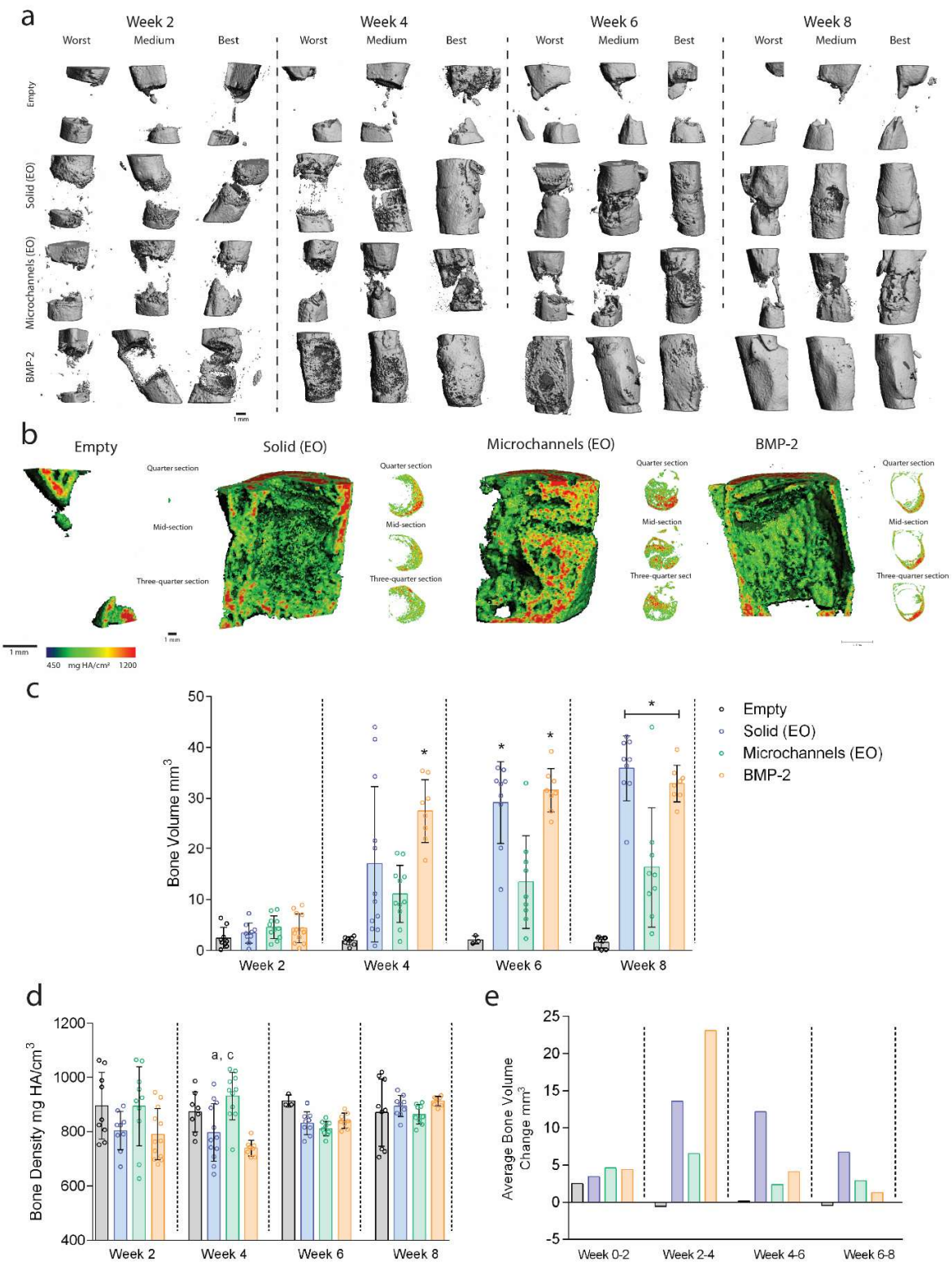
a
Week 2
Week 4
Week 6
Week 8
Worst
Medium
Best
Empty
Solid (EO)
Microchannels (EO)
BMP-2
1 mm
b
Empty
Solid (EO)
Microchannels (EO)
BMP-2
Quarter section
Mid-section
Three-quarter section
1 mm
450 mg HA/cm³ 1200
c
Bone Volume mm³
Week 2
Week 4
Week 6
Week 8
Empty
Solid (EO)
Microchannels (EO)
BMP-2
d
Bone Density mg HA/cm³
a, c
e
Average Bone Volume Change mm³
Week 0-2
Week 2-4
Week 4-6
Week 6-8

Figure 4: µCT analysis of bone formation after 2, 4, 6 & 8 weeks of implantation. (a) Reconstructed *in vivo* µCT analysis of bone formation in the defects, scale-bar 1mm throughout. (b) Representative images of µCT bone densities in the defects at 8 weeks including regional analysis at the defect ¼, ½, and ¾ sections, scale-bar 1mm throughout. (c) Quantification of total bone volume (mm^3) in the defects at each timepoint. (d) Average bone density (mg HA/cm^3) in the defects at each timepoint. . (e) Bone volume change (mm^3) between each timepoint for all groups. Throughout minimum n=9 (except for BMP-2 week 6 & 8 as one animal died at week 5 (n=8) & empty week 6 where the CT machine failed during scanning (n=3)), (mean ± SD) throughout, significance defined as $p < 0.05$ (ANOVA, tukey post-test). a=significance compared to solid (EO), b= significance compared to microchanneled (EO), and c= significance compared to BMP-2 delivery, all for the corresponding timepoint.

To determine whether the incorporation of 3D printed microchannels altered the levels of heterotopic bone formation, ROI bone volume analysis was performed on the week 8 reconstructions. The total bone volume was quantified in the core, annulus, and heterotopic regions of the defect (Fig 5 b). The highest annular bone volume formed in the solid (EO) group, while the microchannels (EO) group supported significantly lower levels of heterotopic bone formation (Fig 5 b). In addition, the solid (EO) group also produced lower levels of heterotopic bone formation compared to BMP-2 delivery (mean values 14.9 ± 3.47 mm^3 vs. 9 ± 4.91 mm^3) (Fig 5b).

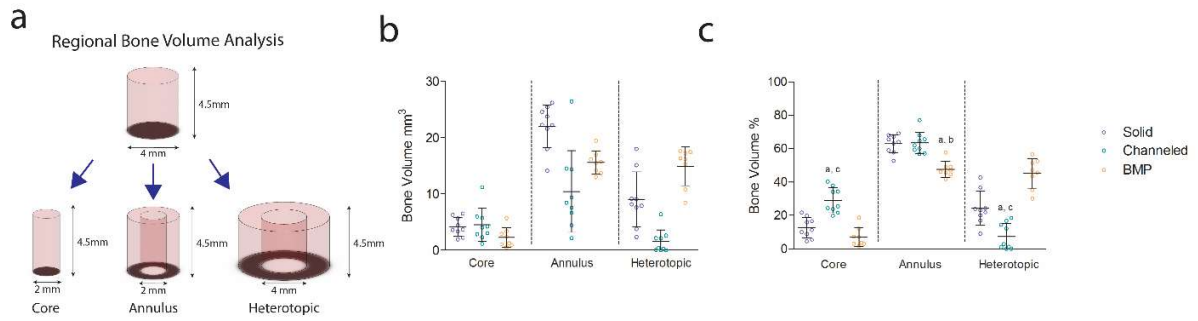

Figure 5: Regional µCT analysis of bone formation. (a) Outline of region of interest bone volume analysis including definitions of core, annulus, and hetertopic regions. (b) Total bone volume (mm^3) in each region at 8 weeks. (c) Bone volume % in each region (regional bone volume/total bone volume) at 8 weeks. All graphs n=8-9 (mean ± SD) throughout, significance defined as $p < 0.05$ (ANOVA, tukey post-test). a = significance compared to solid (EO), b =

significance compared to microchanneled (EO), and c = significance compared to BMP-2 delivery, all for the corresponding timepoint.

3.4 Histological and immunohistochemical analysis of implant vascularisation and endochondral bone formation

To study the progression of endochondral ossification within the defects we performed histological and immunohistochemical staining at 4 & 8 weeks (Fig 6). H&E staining after 4 & 8 weeks revealed bone formation within all groups (Fig 6 a, b). Interestingly, the GelMA hydrogel remained relatively intact and undegraded for the solid cartilage and BMP-2 groups, and bone formation in these groups was predominantly found around the GelMA hydrogel with little bone formation evident inside the gels. Macroscopic images of the sliced constructs before histological processing also confirmed the presence of undegraded GelMA in the solid (EO) and BMP-2 delivery groups (supplementary Fig 2). In contrast, in the microchanneled group the hydrogel appeared more degraded after 4 & 8 weeks, and it was clear that host cells from the marrow and surrounding muscle had invaded via the microchannel network (Fig 6 a, b). The microchannels were filled with tissue that connected with both the two bony ends and surrounding muscle tissue. It should also be noted that areas of GelMA close to a free surface of the construct appeared more degraded. For example, central regions of the solid constructs were wholly intact, whereas the outer surface had started to degrade (Fig 6 a, b). Within both chondrogenically primed groups, safarin-O staining for sGAG, and positive collagen type II staining, demonstrated cartilage tissue was still present in the defects after 4 weeks (Fig 6 a). After 8 weeks, weaker staining for both sGAG and collagen type II, along with positive collagen X staining, indicated repair following implantation of the cartilage templates was proceeding along an endochondral pathway (Fig 6 a, b). It should be noted that positive staining for collagen II was present in the repair tissue that had

filled the microchannels at 4 & 8 weeks (Fig 6 a, b). For the BMP-2 delivery group, negligible staining for sGAG, collagen II or collagen X was present inside the GelMA network after 4 or 8 weeks (Fig 6 a, b). However, it should be noted that some weaker staining for sGAG and collagen II was present in the repaired bone tissue that surrounded residual GelMA hydrogel (Fig 6 a, b).

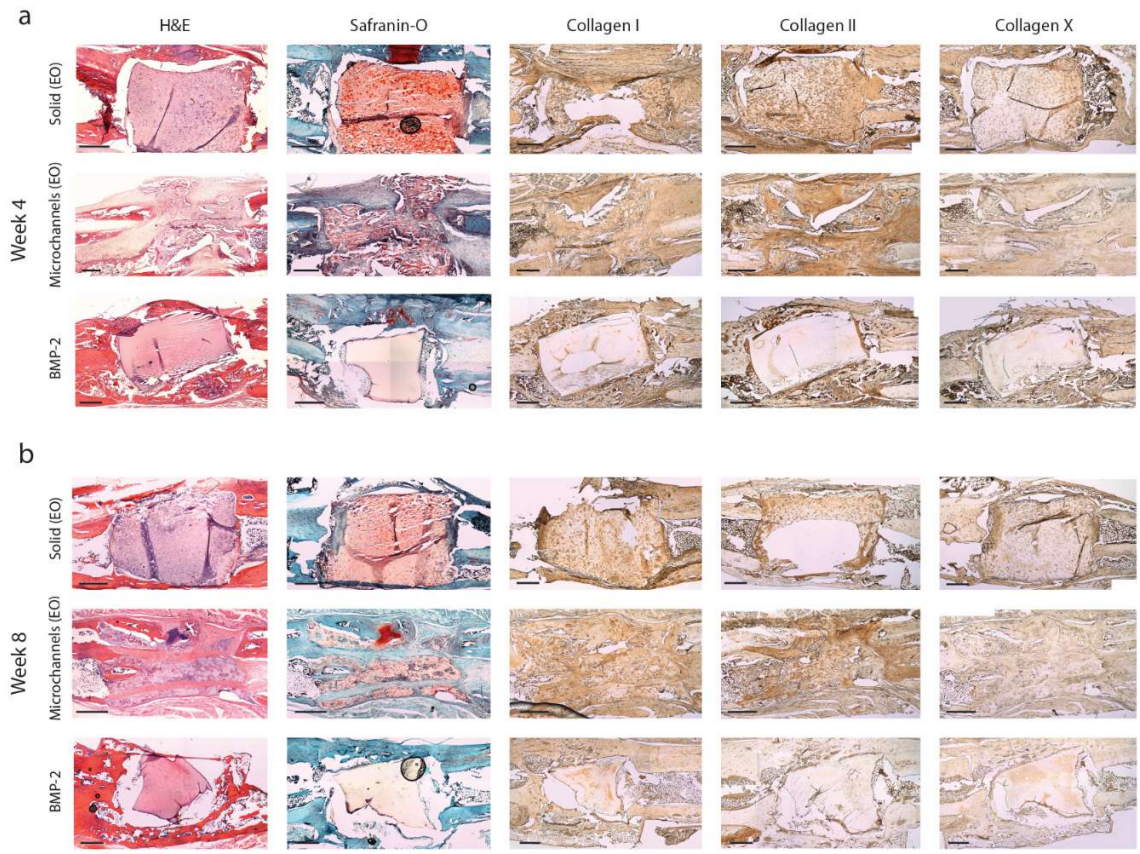

Figure 6: Histological and immunohistochemical staining of defects after 4 & 8 weeks of implantation. H&E staining was used to assess bone formation (intense red/pink staining) and fibrous tissue (weaker pink staining). Safarin-O staining (red staining) for sGAG and immunohistochemical staining for collagen I, II, & X were used to assess the synthesis of cartilage matrix components (n=2). Images (2X stitches) represent the whole defect, scale-bar 1mm throughout. (n=4 for H&E & safarin-O, n=2 for all immune staining)

Next, to assess the levels of vascularisation inside the defect at 8 weeks, distinct areas of red blood cell activity, stained using H&E, were quantified histomorphometrically (Fig 7 a, c).

This revealed that a significantly higher number of blood vessels had invaded the defect after 8 weeks compared to the solid cartilage templates. Next, positive staining for TRAP activity around networks of multinucleated cells, revealed host cells of haematopoietic origin (osteoclasts, macrophages or dendritic cells) had started to degrade the GelMA matrix (Fig 7 b). A higher number of TRAP positive multinucleated cells had invaded the microchanneled cartilage template compared to the other experimental groups (Fig 7 d). No TRAP positive cells were found inside the GelMA hydrogel for the BMP-2 delivery group. Finally, the residual area of GelMA within the defect was quantified histomorphometrically, with the lowest GelMA area found in defects treated with the microchanneled cartilage template while the highest residual GelMA area was found in the BMP-2 group (Fig 7 e).

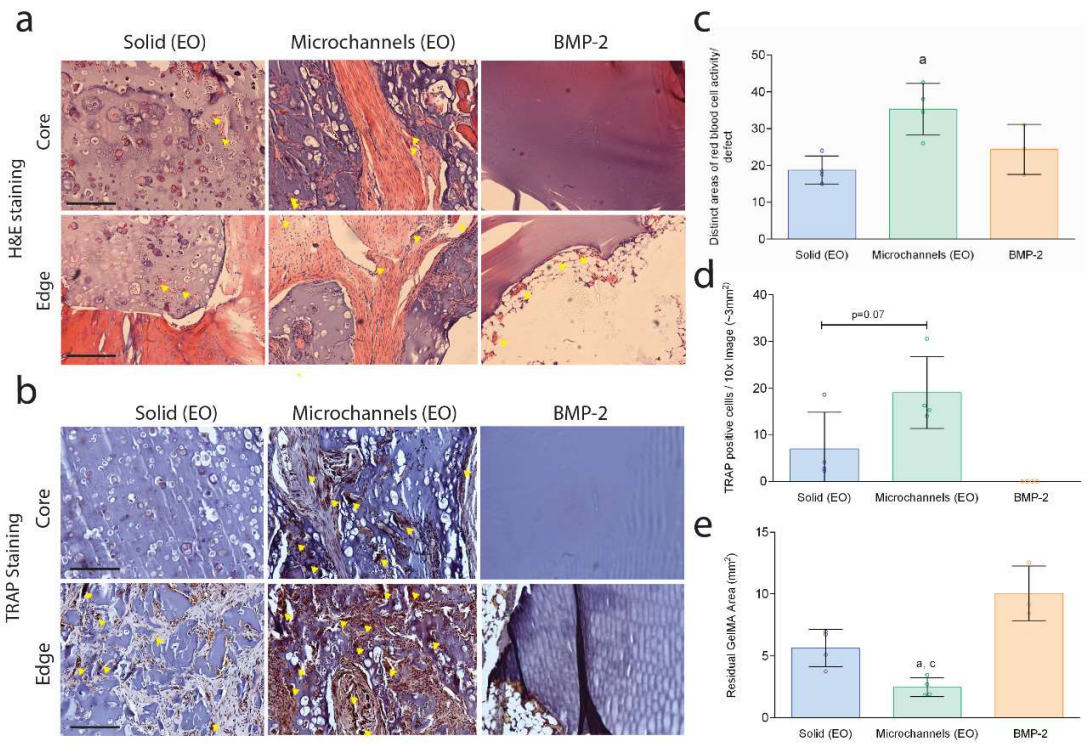

Figure 7: Histological and histomorphometric analysis of host cell invasion after 8 weeks of implantation. (a) H&E staining after 8 weeks in vivo revealing areas of red blood cell activity. Images taken 10X, scale-bar 200µm. (b) Positive

TRAP staining for multinucleated giant cells after 8 weeks in vivo. (c) Histomorphometric quantification of areas of blood vessel within the defect (H&E staining) after 8 weeks in vivo, (n=4 for solid and microchannels, n=3 for BMP-2 as 1 sample was not sufficiently intact to analyse). (d) Histomorphometric quantification of TRAP positive multinucleated giant cells inside the GelMA hydrogel (H&E staining) after 8 weeks in vivo, n=4. (e) Histomorphometric quantification of residual GelMA hydrogel (H&E staining) after 8 weeks in vivo. All graphs (mean ± SD), significance defined as $p < 0.05$ (ANOVA, tukey post-test). a=significance compared to solid (EO), b= significance compared to microchanneled (EO), and c= significance compared to BMP-2 delivery, for the corresponding timepoint. (n=4 for solid and microchannels, n=3 for BMP-2 as 1 sample was not sufficiently intact to analyse)

4 Discussion

The overall goal of this study was to determine whether the incorporation of 3D printed microchannels into engineered cartilage tissues could enhance vascularisation and endochondral bone regeneration following their implantation into critically sized femoral bone defects. The incorporation of microchannels did not enhance overall levels of bone formation, with higher total levels of bone formation observed for the solid cartilage templates; however, their incorporation did have a number of clear advantages. After 4 weeks, μCT angiography demonstrated that the incorporation of microchannels into such engineered templates led to higher levels of vascularisation in core regions of the bone defect. After 8 weeks, histological analysis demonstrated that a higher number of host osteoclast/immune cells had invaded the cartilage template via the microchannel network, which correlated with higher levels of vascularisation and increased degradation of the GelMA hydrogel. Finally, it was demonstrated that the endochondral approach promoted comparable levels of bone formation to BMP-2 delivery, whilst promoting lower levels of heterotopic bone formation, with the lowest levels of heterotopic bone formation observed for the microchanneled cartilage templates. Taken together, these results confirm the potential of endochondral bone tissue engineering and demonstrate that 3D-printed microchannels offer a promising approach for guiding vascularisation and implant remodelling during endochondral bone repair.

In this study we demonstrate a novel approach to engineer cartilage templates containing complex interconnected microchannel networks using 3D printing technology. The approach offers a number of advantages over traditional removal template molding techniques. Firstly, it was possible to modulate the microchannel geometry rapidly by simply changing the printing speed. This is a significant advantage over traditional casting techniques that require new

microfabrication equipment to be produced each time. Secondly, using our printing technique it was possible to introduce bi-directional interconnected channels. This is not possible using casting techniques where the sacrificial component can only be removed along one direction. Typically templates such as straight wires or needles are used which limits design complexity [37]. Although some authors have reported methods to produce bifurcating channels using flexible polydimethylsiloxane (PDMS) rods [38], the need to extract the templates from fragile hydrogels limits the design complexity and microchannel sizes that can be achieved. With our approach it was possible to introduced bi-directional microchannels throughout a 3D construct. This will be particularly advantageous when attempting to repair complex clinical fractures where patient CT data will be available to develop print patterns. The central microchannel diameter was large (900μm), in order to mimic the geometry of the marrow canal. The remaining microchannel diameters (365μm) were motivated by previous studies where channel diameters in the range of 250-500μm have been shown to be optimal for bone tissue engineering [39–41]. For example, the influence of microchannel diameter on bone regeneration was recently explored in an osteochondral defect model by implanting calcium phosphate–collagen scaffolds with aligned microchannels diameters of 140 μm, 270 μm, and 640 μm [42]. The scaffold with 270 μm channels was found to support the highest levels of bone formation and vascularisation. In another study, collagen scaffolds with a mean pore size of 325μm were found optimal for bone tissue engineering [43].

Implantation of engineered cartilage templates was found to accelerate bone healing compared to untreated controls. The endochondral approach to bone repair initiates a cascade of events that mimics key aspects of bone development where temporary cartilaginous templates become vascularised and transformed into bone [14]. Hypertrophic chondrocytes express angiogenic factors such as VEGF, which initiates vascularisation of the cartilage template [44]. The newly formed vessels deliver osteoblasts and osteoprogenitors cells which facilitate mineralisation and bone formation. Interestingly, total bone formation was higher in the solid constructs compared to the microchannels constructs (Fig 4 c). This may be due to fact that the incorporation of microchannels reduced the number of cells delivered into the defect by approximately 30% (Fig 2 b). It has been shown that chondrogenically primed MSCs secrete a cocktail of morphogenic proteins such as VEGF, BMP-2, SDF-1, and PDGF that play key roles in fracture healing [15,18,45]. It is possible that the reduced presence of these factors in the microchanneled group reduced total bone formation. In addition, previous analysis of endochondral bone tissue engineering strategies has demonstrated that the transplanted MSC population participates in bone formation, and bone is formed by both host and transplanted [16,46,47]. For example, Scotti et al 2013 reported on the development on mature bone organs containing both cortical and trabecular structures via endochondral ossification [16]. Interestingly, the outer cortical perichondral bone was formed mainly by host cells, whereas the inner trabecular like bone that was formed mainly by the transplanted cells. The lower levels of bone formation observed in the microchanneled cartilage template could also be due to the fact that less transplanted cells were available to participate in bone formation. Notwithstanding the above, whether the solid constructs are actually out-performing channelled constructs is a point of debate. Clearly, overall levels of bone formation are lower, however vascularization is higher and ectopic

bone formation is lower. It could be argued that lower levels of well vascularized bone, which forms within the actual defect area, is in fact a more desirable outcome. Future work in larger bone defect models will look to develop 3D printed microchanneled cartilage templates containing a higher number of MSCs in an attempt to further accelerate bone formation. For example, this could be achieved by simply increasing the MSC density in the solid phase of the construct.

Before endochondral repair strategies can be used to treat bone defects in a clinical setting, a significant geometrical scaling up of existing *in vitro* cartilage tissue engineering strategies will be required. For example, an attempt to engineer whole bone organs via endochondral ossification highlighted these challenges with core regions of the pre-cursor cartilage templates devoid of cells and matrix after the *in vitro* culture period [16]. The system developed here is a promising approach to overcome these limitations as it has been shown that microchannels can enhance act as conduits for nutrient transport during the *in vitro* culture, helping to facilitate the scaling up of cartilage tissue engineering strategies [48,49]. The successful scaling up of endochondral bone repair strategies will also require the cartilage templates to become rapidly vascularised upon implantation *in vivo.* Here, we demonstrate the incorporation of microchannels is a promising approach to guide vascularisation within core regions during bone defect healing. In contrast, the levels of bone formation and vascularisation were low in core regions of defects treated with the solid tissues. This would be a significant limitation in larger defect models where much larger volumes of cartilage will require rapid vascularisation. The ability to guide vascularisation could also provide a way to customise the implant to match the local vascular architecture.

A key consideration for any endochondral bone repair strategy is the choice of hydrogel or scaffold used to engineer the cartilage precursor. While a number hydrogels such as alginate [22,24,50], chitosan [50], fibrin [25,50], GelMA [17,24], and agarose [51] have all been explored

for their capacity to support endochondral bone formation, these studies have all been performed in a subcutaneous environment within immune compromised animals that lack a relevant immune reaction. As such we wanted to assess the feasibility of hydrogel based endochondral bone repair strategies in an orthotopic model. We chose to use GelMA for a number of reasons. Firstly, GelMA is matrix metalloproteinase (MMP) sensitive, and can support cell mediated degradation [37,52–54]. Secondly, it has been demonstrated that endothelial colony forming cells (ECFCs) are capable of undergoing angiogenesis and vasculogenesis in GelMA hydrogels both *in vitro* and *in vivo* [53]. Finally, GelMA is also a widely used bioink for 3D bioprinting which will make it possible to fully integrate our approach with cell bioprinting [28,55]. Interestingly, in our orthotopic model the solid GelMA hydrogel remained largely undegraded after 8 weeks. In both the solid and BMP-2 groups, although the defects were fully bridged, a large volume of undegraded hydrogel remained in the centre of the defect. This highlights the challenges faced when employing hydrogels for endochondral bone tissue engineering strategies.

Promoting interaction between the implanted cartilage graft and the host has been shown to be a key consideration for endochondral bone repair strategies [56]. Here, for all histological staining it was evident that the incorporation of printed microchannels enhanced host interaction *in vivo*. Four and eight weeks post-implantation, the GelMA hydrogel remained relatively intact for the solid (EO) group, whereas for the microchannels (EO) group the hydrogel was more broken down (Fig 6 a, b). It was clear that host cells from the marrow and surrounding muscle had invaded via the microchannel network, as host tissue had formed in the radial and longitudinal microchannels which connected with both the two bony ends, and the surrounding muscle tissue (see arrows in figure 6 b, H&E staining). It should also be noted that areas of the GelMA hydrogel closer to a free surface appeared more degraded. For example, central regions of the solid

constructs were wholly intact, whereas at the outer surface degradation was evident (Fig 6 a, b). This supports the hypothesis that enhancing host interaction with the incorporation of microchannels could enhance clearance of the hydrogel network. In addition, the lowest area of residual GelMA was found in the microchanneled cartilage template (Fig 7 e). As well as this, a larger number of TRAP positive cells were present in this engineered cartilage template at 8 weeks (Fig 7 d). The enhanced hydrogel degradation is possibly due to the increased invasion of host immune cells, such as macrophages, that play a key role in degrading gelatin hydrogels [57]. A number of other approaches could be explored to accelerate the degradation rate of the GelMA hydrogel. For example, lowering the degree of metacrylation can accelerate degradation rate of GelMA *in vivo* [53,58]. In addition, lowering the macromer concentration can also accelerate the degradation rate of the hydrogel [37]. However, we have found that macromer concentrations lower than 10%, the concentration used in this study, results in hydrogels that are very soft and difficult to handle. Recently thiol-ene clickable gelatin bioinks that photo-polymerise in step-growth manner have been developed [59]. These inks possess a more idealised network structure compared to methacrylated gelatin, where free-radical chain-growth results in the formation of undegradable high molecular weight components. Thiol-ene clickable hydrogels can also be crosslinked using cysteine-flanked degradable matrix metalloproteinase (MMP) peptides [60]. Future work will look to integrate thiol-ene clickable gelatins with the 3D-printing approach developed here to further improve endochondral bone tissue engineering strategies.

In this study, we demonstrate that an endochondral bone tissue engineering strategy can support comparable levels of bone healing to high dose BMP-2 delivery (0.2 mg/ml GelMA solution). In addition, we also demonstrate that compared to high dose BMP-2 delivery the endochondral approach results in lower levels of heterotopic bone formation (Fig 5 b). This

demonstrates that the endochondral approach to bone repair offers a promising and potentially safer alternative to BMP-2 delivery. This supra-physiological dose is comparable to the off-label high-dose often used clinically [61]. Interestingly, the highest levels of new bone formation occurred between 2 and 4 weeks for this group, and then plateaued between week 4 and 8 (Fig 4 e). In contrast, the rate of new bone formation for the solid (EO) group were consistent throughout the study, eventually catching up to the BMP-2 group after 8 weeks. The higher levels of early bone formation may be due to the fact the BMP-2 delivery group induced a more direct intramembranous repair process. It is believed that BMP-2 induced repair occurs at least partially via an intramembranous pathway, as previous studies have reported the absence of cartilage tissue at earlier timepoints during bone defect healing [2,62]. However, it should be noted that some weak staining for cartilage-like tissue was present in our BMP-2 delivery group after 4 weeks, which is suggestive of an endochondral contribution to the repair process. This is in agreement with previous studies using higher doses of BMP-2 that have also reported some evidence of endochondral bone formation in femoral fracture models [3].

The framework developed in this study would likely encounter a number of challenges before it could be adopted in a clinical setting. For example, implementing an autologous approach would first require isolating MSCs from the patient. Then it would be necessary to expand these cells for a number of passages in order to obtain a sufficient amount of cells to engineer a template to treat a large bone defect. There are significant costs and regulatory challenges associated with such a strategy. However, it should be noted that a number of pre-clinical studies in humans have reported on the feasibility of repairing large bone defects using pre-cultured scaffolds loaded with culture expanded BMSCs [63,64]. While clinical translation may be hampered due to the extra costs that would be necessary to isolate, expand, and chondrogenically prime the cartilage

template, it should be noted that recently more translatable endochondral approaches have been developed. For example, devitalised cartilage templates [45], decellularised hypertrophic cartilage scaffolds [36] and growth plate derived scaffolds [65] all offer promising "off-the-shelf" approaches for driving endochondral bone formation that could potentially be improved by using 3D printing to engineer smart implant geometries.

5 Conclusion

Although endochondral bone tissue engineering offers a promising route to repair, achieving robust vascularisation is a major challenge with these approaches. Our 3D printed microchannel networks represent a versatile and scalable approach to guide vascularisation during endochondral bone repair. While higher levels of total bone formation were observed following implantation of the solid templates, increased vascularization and implant remodelling was observed in channelled templates, and we anticipate their inclusion will be necessary to facilitate the scaling up of endochondral bone repair strategies toward clinical relevance, where the problem of ensuring adequate vascularisation is exacerbated. In addition, it will be possible to integrate this approach with patient specific data to engineer patient-specific implants. This could make it possible to direct vascularisation and bone formation in complex bone fractures that are often observed clinically. Finally, we demonstrate that our endochondral approach to bone repair can support comparable levels of bone healing to the clinically adopted BMP-2 delivery, whilst supporting lower levels of heterotopic bone formation.

6 References

1. Betz RR. Limitations of autograft and allograft: new synthetic solutions. *Orthopedics* 2002;**25**:561–70.

2. Priddy LB, Chaudhuri O, Stevens HY *et al.* Oxidized alginate hydrogels for bone morphogenetic protein-2 delivery in long bone defects. *Acta Biomater* 2014;**10**:4390–9.

3. Krishnan L, Priddy LB, Esancy C *et al.* Delivery vehicle effects on bone regeneration and heterotopic ossification induced by high dose BMP-2. *Acta Biomater* 2017;**49**:101–12.

4. Yasko AW, Lane JM, Fellinger EJ *et al.* The healing of segmental bone defects , induced by recombinant human bone morphogenetic protein (rhBMP-2). *J Bone Jt Surg* 2009;**74**:659–70.

5. Gerhart TN, Kirker-Head CA, Kriz MJ *et al.* Healing segmental femoral defects in sheep using recombinant human bone morphogenetic protein. *Clin Orthop Relat Res* 1993;**Aug**:317–26.

6. Martin GJ, Boden SD, Marone M a *et al.* Posterolateral intertransverse process spinal arthrodesis with rhBMP-2 in a nonhuman primate: important lessons learned regarding dose, carrier, and safety. *J Spinal Disord* 1999;**12**:179–86.

7. Zara JN, Siu RK, Zhang X *et al.* High Doses of Bone Morphogenetic Protein 2 Induce Structurally Abnormal Bone and Inflammation *In Vivo*. *Tissue Eng Part A* 2011;**17**:1389–99.

8. Boerckel JD, Kolambkar YM, Dupont KM *et al.* Effects of protein dose and delivery system on BMP-mediated bone regeneration. *Biomaterials* 2011;**32**:5241–51.

9. Hustedt JW, Blizzard DJ. The controversy surrounding bone morphogenetic proteins in the spine: A review of current research. *Yale J Biol Med* 2014;**87**:549–61.

10. Ong KL, Villarraga ML, Lau E *et al.* Off-label use of bone morphogenetic proteins in the United States using administrative data. *Spine (Phila Pa 1976)* 2010;**35**:1794–800.

11. Shields LBE, Raque GH, Glassman SD *et al.* Adverse effects associated with high-dose recombinant human bone morphogenetic protein-2 use in anterior cervical spine fusion. *Spine (Phila Pa 1976)* 2006;**31**:542–7.

12. Tannoury CA, An HS. Complications with the use of bone morphogenetic protein 2 (BMP-2) in spine surgery. *Spine J* 2014;**14**:552–9.

13. Deutsch H. High-dose bone morphogenetic protein-induced ectopic abdomen bone growth. *Spine J* 2010;**10**:e1–4.

14. Thompson EM, Matsiko A, Farrell E *et al.* Recapitulating endochondral ossification: A promising route to in vivo bone regeneration. *J Tissue Eng Regen Med* 2015;**9**:889–902.

15. Scotti C, Tonnarelli B, Papadimitropoulos A *et al.* Recapitulation of endochondral bone formation using human adult mesenchymal stem cells as a paradigm for developmental engineering. *Proc Natl Acad Sci* 2010;**107**:7251–6.

16. Scotti C, Piccinini E, Takizawa H *et al.* Engineering of a functional bone organ through endochondral ossification. *Proc Natl Acad Sci* 2013;**110**:3997–4002.

17. Visser J, Gawlitta D, Benders KEM *et al.* Endochondral bone formation in gelatin methacrylamide hydrogel with embedded cartilage-derived matrix particles. *Biomaterials* 2015;**37**:174–82.

18. Thompson EM, Matsiko A, Kelly DJ *et al.* An Endochondral Ossification-Based Approach to Bone Repair: Chondrogenically Primed Mesenchymal Stem Cell-Laden Scaffolds Support Greater

Repair of Critical-Sized Cranial Defects Than Osteogenically Stimulated Constructs *In Vivo*. *Tissue Eng Part A* 2016;**22**:556–67.

19. Huang JI, Durbhakula MM, Angele P *et al.* Lunate arthroplasty with autologous mesenchymal stem cells in a rabbit model. *J Bone Joint Surg Am* 2006;**88**:744–52.

20. Harada N, Watanabe Y, Sato K *et al.* Bone regeneration in a massive rat femur defect through endochondral ossification achieved with chondrogenically differentiated MSCs in a degradable scaffold. *Biomaterials* 2014;**35**:7800–10.

21. van der Stok J, Koolen MKE, Jahr H *et al.* Chondrogenically differentiated mesenchymal stromal cell pellets stimulate endochondral bone regeneration in critical-sized bone defects. *Eur Cells Mater* 2014;**27**:137–48.

22. Cunniffe GM, Vinardell T, Thompson EM *et al.* Chondrogenically primed mesenchymal stem cell-seeded alginate hydrogels promote early bone formation in critically-sized defects. *Eur Polym J* 2015;**72**:464–72.

23. Bernhard J, Ferguson J, Rieder B *et al.* Tissue-engineered hypertrophic chondrocyte grafts enhanced long bone repair. *Biomaterials* 2017;**139**:202–12.

24. Daly AC, Cunniffe GM, Sathy BN *et al.* 3D Bioprinting of Developmentally Inspired Templates for Whole Bone Organ Engineering. *Adv Healthc Mater* 2016;**5**:2353–62.

25. Sheehy EJ, Mesallati T, Kelly L *et al.* Tissue Engineering Whole Bones Through Endochondral Ossification: Regenerating the Distal Phalanx. *Biores Open Access* 2015;**4**:229–41.

26. Mesallati T, Sheehy EJ, Vinardell T *et al.* Tissue engineering scaled-up, anatomically shaped osteochondral constructs for joint resurfacing. *Eur Cells Mater* 2015;**30**:163–86.

27. Murphy S V, Atala A. 3D bioprinting of tissues and organs. *Nat Biotechnol* 2014;**32**:773–85.

28. Daly AC, Freeman FE, Gonzalez-Fernandez T *et al.* 3D Bioprinting for Cartilage and Osteochondral Tissue Engineering. *Adv Healthc Mater* 2017;**1700298**:1700298.

29. Malda J, Visser J, Melchels FP *et al.* 25th anniversary article: Engineering hydrogels for biofabrication. *Adv Mater* 2013;**25**:5011–28.

30. Miller JS, Stevens KR, Yang MT *et al.* Rapid casting of patterned vascular networks for perfusable engineered three-dimensional tissues. *Nat Mater* 2012;**11**:768–74.

31. Van Den Bulcke AI, Bogdanov B, De Rooze N *et al.* Structural and Rheological Properties of Methacrylamide Modified Gelatin Hydrogels. *Biomacromolecules* 2000;**1**:31–8.

32. Shin H, Olsen BD, Khademhosseini A. The mechanical properties and cytotoxicity of cell-laden double-network hydrogels based on photocrosslinkable gelatin and gellan gum biomacromolecules. *Biomaterials* 2012;**33**:3143–52.

33. Lee BH, Shirahama H, Cho N-J *et al.* Efficient and controllable synthesis of highly substituted gelatin methacrylamide for mechanically stiff hydrogels. *RSC Adv* 2015;**5**:106094–7.

34. Bohorquez M, Koch C, Trygstad T *et al.* A Study of the Temperature-Dependent Micellization of Pluronic F127. *J Colloid Interface Sci* 1999;**216**:34–40.

35. Filion TM, Li X, Mason-Savas A *et al.* Elastomeric Osteoconductive Synthetic Scaffolds with Acquired Osteoinductivity Expedite the Repair of Critical Femoral Defects in Rats. *Tissue Eng Part A* 2011;**17**:503–11.

36. Cunniffe GM, Vinardell T, Murphy JM *et al.* Porous decellularized tissue engineered

hypertrophic cartilage as a scaffold for large bone defect healing. *Acta Biomater* 2015;**23**:82–90.

37. Nichol JW, Koshy ST, Bae H *et al.* Cell-laden microengineered gelatin methacrylate hydrogels. *Biomaterials* 2010;**31**:5536–44.

38. Jiménez-Torres JA, Peery SL, Sung KE *et al.* LumeNEXT: A Practical Method to Pattern Luminal Structures in ECM Gels. *Adv Healthc Mater* 2016;**5**:198–204.

39. Tsuruga E, Takita H, Itoh H *et al.* Pore size of porous hydroxyapatite as the cell-substratum controls BMP-induced osteogenesis. *J Biochem* 1997;**121**:317–24.

40. Kühne JH, Bartl R, Frisch B *et al.* Bone formation in coralline hydroxyapatite. Effects of pore size studied in rabbits. *Acta Orthop Scand* 1994;**65**:246–52.

41. Amini AR, Laurencin CT, Nukavarapu SP. Bone Tissue Engineering: Recent Advances and Challenges. *Crit Rev Biomed Eng* 2012;**40**:363–408.

42. Seong YJ, Kang IG, Song EH *et al.* Calcium Phosphate-Collagen Scaffold with Aligned Pore Channels for Enhanced Osteochondral Regeneration. *Adv Healthc Mater* 2017;**1700966**:1–11.

43. Murphy CM, Haugh MG, O'Brien FJ. The effect of mean pore size on cell attachment, proliferation and migration in collagen-glycosaminoglycan scaffolds for bone tissue engineering. *Biomaterials* 2010;**31**:461–6.

44. Studer D, Millan C, Maniura-weber K *et al.* Molecular and Biophysical Mechanisms Regulating Hypertrophic. *Eur Cells Mater* 2012;**24**:118–35.

45. Bourgine PE, Scotti C, Pigeot S *et al.* Osteoinductivity of engineered cartilaginous templates devitalized by inducible apoptosis. *Proc Natl Acad Sci* 2014;**111**:17426–31.

46. Tortelli F, Tasso R, Loiacono F *et al.* The development of tissue-engineered bone of different origin through endochondral and intramembranous ossification following the implantation of mesenchymal stem cells and osteoblasts in a murine model. *Biomaterials* 2010;**31**:242–9.

47. Farrell E, Both SK, Odörfer KI *et al.* In-vivo generation of bone via endochondral ossification by in-vitro chondrogenic priming of adult human and rat mesenchymal stem cells. *BMC Musculoskelet Disord* 2011;**12**:31.

48. Cigan AD, Durney KM, Nims RJ *et al.* Nutrient Channels Aid the Growth of Articular Surface-Sized Engineered Cartilage Constructs. *Tissue Eng Part A* 2016;**22**:1063–71.

49. Daly AC, Sathy BN, Kelly DJ *et al.* Engineering large cartilage tissues using dynamic bioreactor culture at defined oxygen conditions Corresponding author : *J Tissue Eng* 2018;**In press**,

50. Sheehy EJ, Mesallati T, Vinardell T *et al.* Engineering cartilage or endochondral bone: A comparison of different naturally derived hydrogels. *Acta Biomater* 2015;**13**:245–53.

51. Sheehy EJ, Vinardell T, Toner ME *et al.* Altering the architecture of tissue engineered hypertrophic cartilaginous grafts facilitates vascularisation and accelerates mineralisation. *PLoS One* 2014;**9**:e90716.

52. Yue K, Trujillo-de Santiago G, Alvarez MM *et al.* Synthesis, properties, and biomedical applications of gelatin methacryloyl (GelMA) hydrogels. *Biomaterials* 2015;**73**:254–71.

53. Chen YC, Lin RZ, Qi H *et al.* Functional human vascular network generated in photocrosslinkable gelatin methacrylate hydrogels. *Adv Funct Mater* 2012;**22**:2027–39.

54. Jia W, Gungor-Ozkerim PS, Zhang YS *et al.* Direct 3D bioprinting of perfusable vascular

constructs using a blend bioink. *Biomaterials* 2016;**106**:58–68.

55. Bertassoni LE, Cardoso JC, Manoharan V *et al.* Direct-write bioprinting of cell-laden methacrylated gelatin hydrogels. *Biofabrication* 2014;**6**, DOI: 10.1088/1758-5082/6/2/024105.

56. Bahney CS, Jacobs L, Tamai R *et al.* Promoting Endochondral Bone Repair Using Human Osteoarthritic Articular Chondrocytes. *Tissue Eng Part A* 2016;**22**:427–35.

57. Kim YH, Furuya H, Tabata Y. Enhancement of bone regeneration by dual release of a macrophage recruitment agent and platelet-rich plasma from gelatin hydrogels. *Biomaterials* 2014;**35**:214–24.

58. Byambaa B, Annabi N, Yue K *et al.* Bioprinted Osteogenic and Vasculogenic Patterns for Engineering 3D Bone Tissue. *Adv Healthc Mater* 2017;**6**:1–15.

59. Bertlein S, Brown G, Lim KS *et al.* Thiol-Ene Clickable Gelatin: A Platform Bioink for Multiple 3D Biofabrication Technologies. *Adv Mater* 2017;**1703404**, DOI: 10.1002/adma.201703404.

60. Lutolf MP, Hubbell JA. Synthesis and physicochemical characterization of end-linked poly(ethylene glycol)-co-peptide hydrogels formed by Michael-type addition. *Biomacromolecules* 2003;**4**:713–22.

61. Fu R, Selph S, McDonagh M *et al.* Effectiveness and Harms of Recombinant Human Bone Morphogenetic Protein-2 in Spine Fusion. *Ann Intern Med* 2013;**158**:890.

62. Kolambkar YM, Dupont KM, Boerckel JD *et al.* An alginate-based hybrid system for growth factor delivery in the functional repair of large bone defects. *Biomaterials* 2011;**32**:65–74.

63. RODOLFO Q, MADDALENA M, RANIERI C *et al.* Repair of Large Bone Defects with the USe of Autologous Bone Marrow Stromal Cells. *N Engl J Med* 2001;**344**.

64. Morishita T, Honoki K, Ohgushi H *et al.* Tissue Engineering Approach to the Treatment of Bone Tumors: Three Cases of Cultured Bone Grafts Derived From Patients' Mesenchymal Stem Cells. *Artif Organs* 2006;**30**:115–8.

65. Cunniffe GM, Díaz-Payno PJ, Ramey JS *et al.* Growth plate extracellular matrix-derived scaffolds for large bone defect healing. *Eur Cells Mater* 2017;**33**:130–42.

7 Supplementary Figures

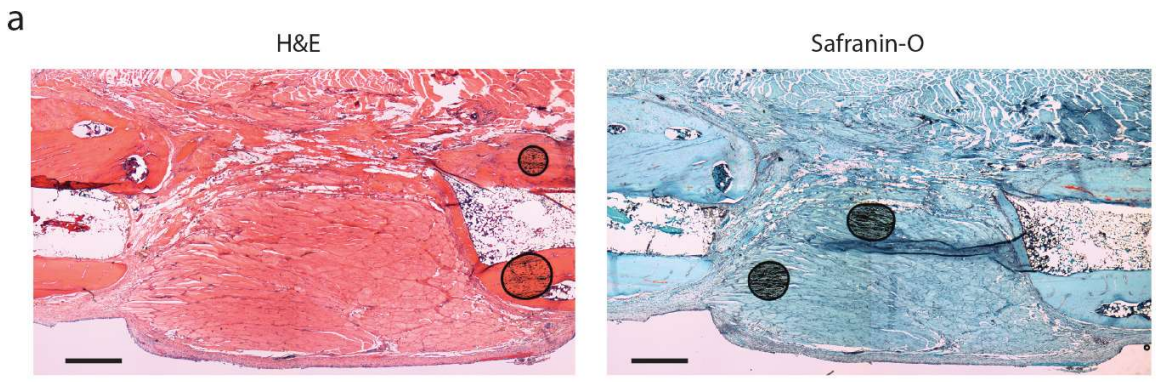

Supplementary figure 1: (a) Histological staining of defects after 8 weeks of implantation. H&E staining was used to assess bone formation (intense red/pink staining) and fibrous tissue (weaker pink staining). Safarin-O staining (red staining) for sGAG. Images (2X stitches) represent the whole defect, scale-bar 1mm throughout.

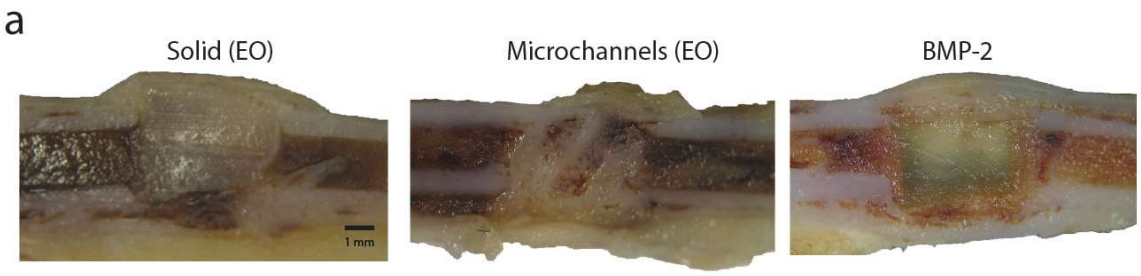

Supplementary figure 2: Macroscopic images of sliced constructs post-fixing at 8 weeks, scale-bar 1mm.

8 Acknowledgements

This publication has emanated from research supported by a research grant from Science Foundation Ireland (SFI) under Grant Number 12/IA/1554 and a European Research Council Starter grant (258463). We would also like to thank Ciaran Gavagan (Trinity College Dublin) for his assistance during animal surgeries.

9 Competing interests

The authors have no competing interests to declare.